Eleventh International Conference on Computational Fluid Dynamics (ICCFD11), Maui, Hawaii, July 11-15, 2022

ICCFD11-4001

Multi-Resolution Analysis of Partially-Stirred Reactor Models for Subgrid Turbulence / Chemistry Interactions

J. Edwards*, C. Ragath* and A. Navratil*
Corresponding author: jredward@ncsu.edu

* North Carolina State University, Raleigh, NC, USA

Abstract: A multi-resolution analysis (MRA) technique in which coupled sequences of LES simulations are solved on successively coarsened meshes is used to analyze the relative performance of several algebraic partially-stirred reactor (PaSR) subgrid models for turbulent combustion. The test case is a methane-hydrogen bluff-body flame, and the 'truth solution' is obtained from a fine-mesh LES that resolves the flow into the dissipative scales. The velocity field from this solution drives the solutions obtained on the underlying coarser meshes, enabling a tight correlation of eddy structures. Conditional distributions of chemical production rate norms and local heat release over a subgrid Reynolds-number / Damköhler sample space are extracted from each coarse-mesh level. The results show that none of the tested PaSR methods accurately predicts the combustion characteristics evidenced from the finest mesh; results improve when coupling with an 'outer environment' is included. Optimal forms for the characteristic PaSR time scale and fine-scale volume fraction are regressed from the data and can be modeled effectively using resolved scale information. The use of these forms provides improved results and yields a level of mesh-independence that is not found in the original algebraic PaSR models.

Keywords: Turbulent Combustion, Large-Eddy Simulation,

1 Introduction

The quest for an economical, accurate method to model the effects of unresolved turbulent fluctuations on finite rates of chemical production is a pacing issue in large-eddy simulation of turbulent combustion. Several groups [1-3] have successfully utilized partially-stirred reactor (PaSR) concepts to model subgrid effects. This work focuses on the evaluation of some of these closures using a multi-resolution analysis technique developed at NCSU. This approach, termed *Multi-Resolution Analysis using Mesh-Sequenced Realizations* (MRA-MSR), henceforth denoted as MRA for brevity [4], performs simultaneous large-eddy (or direct numerical) simulations on a hierarchy of mesh levels. The velocity field on coarser mesh levels is constrained using a relaxation-type source term dependent on the filtered data from the finest mesh – this allows the eddy structures on all mesh levels to be correlated in space and time. At a given coarser scale, complete subgrid information is available for use in assessing turbulence-chemistry interaction (TCI) closure postulates applied at that scale. We have used this capability to develop a new class of TCI subgrid models [5] and to assess other aspects of TCI, such as the presence of a degree of scale-similarity in chemical time scale distributions for non-premixed flames [4]. In this work, we use MRA to assess the performance of various PaSR concepts from the literature and to progress toward optimized forms that may provide improved performance. The remainder of this abstract first presents a generalized description of transport-equation based PaSR closures, then simplifies this description to the algebraic forms most commonly applied. Specific examples from the

literature are then assessed using an existing MRA database [4] (developed for one of the Sydney bluff-body stabilized methane-hydrogen flames.

2 Problem Statement

2.1 A Generalized PaSR Description

A generalization of PaSR subgrid-modeling concepts involves the solution of the following transport equation for a particular scale *k* within the subgrid domain:

$$\frac{\partial(\rho_s^{(k)}\alpha_k)}{\partial t}+\frac{\partial(\rho_s^{(k)}\alpha_k\tilde{u}_j)}{\partial x_j}+\frac{1}{\Omega}\sum_{m=k-1}^{k+1}(\rho_s^{(k)}[(\vec{v}'\cdot\vec{n})_{(km)}^{+}+v_d^{(km)}]+\rho_s^{(m)}[(\vec{v}'\cdot\vec{n})_{(km)}^{-}-v_d^{(km)}])A_{(km)} \quad (1)$$
$$=\alpha_k\dot{\omega}_s(\rho_s^{(k)},T^{(k)}),\ k=1,N$$

Here, (triadic) interactions between scale *k* and scales just larger (*m* = *k*-1) and smaller (*m* = *k*+1) are considered. Transport across the surface area $A_{(km)}$ due to subgrid-scale turbulence and molecular diffusion is quantified by $(\vec{v}'\cdot\vec{n})_{(km)}^{\pm}\pm v_d^{(km)}$, while changes in *k*-class species mass due to chemical reaction are represented by $\alpha_k\dot{\omega}_s\Omega$, where Ω is the volume of the cutoff scale ($\Omega=\Delta^3$). The quantity α_k is the volume fraction of *k*-class structures – a measure of their population and size. The surface-to-volume ratio $A_{(km)}/(\alpha_k\Omega)$ is a measure of *k*-class structure topology, while $\vec{n}_{(km)}$ is the average orientation of a *k*-class structure. If one assumes that subgrid-scale transport can be modeled as $\vec{v}'^{\pm}=\pm|\vec{v}'\cdot\vec{n}|\vec{n}$ and that $\rho_s^{(k)}=\bar{\rho}Y_s^{(k)}$, Eq. (1) becomes

$$\frac{\partial(\bar{\rho}Y_s^{(k)}\alpha_k)}{\partial t}+\frac{\partial(\bar{\rho}Y_s^{(k)}\alpha_k\tilde{u}_j)}{\partial x_j}+\frac{1}{\Omega}\sum_{m=k-1}^{k+1}\bar{\rho}[|\vec{v}'\cdot\vec{n}|_{(km)}+v_d^{(km)}](Y_s^{(k)}-Y_s^{(m)})A_{(km)}=\alpha_k\dot{\omega}_s(\bar{\rho},Y_s^{(k)},T^{(k)}) \quad (2)$$

This equation may be summed over all scales *k* to yield the species conservation equation at the cutoff scale, leading to the closure rules $\tilde{Y}_s=\sum_k Y_s^{(k)}\alpha_k$ and $\sum_k\alpha_k=1$. These can be used to express $Y_s^{(m)}$ in terms of the filtered mean data at the cutoff scale:

$$Y_s^{(m)}=(\tilde{Y}_s-\sum_{l,l\neq m}Y_s^{(l)}\alpha_l)/(1-\sum_{l,l\neq m}\alpha_l) \quad (3)$$

Further simplifications and assumptions can be applied to reduce the system to an algebraic form. Assuming that turbulence structures at small scales are notionally represented as vortex tubes with the longer dimension of the order of the cutoff scale, then $A_{(km)}/(\alpha_k\Omega)\sim(n_k\Delta L_{km})/(n_k\Delta L_{km}^2)\sim 1/L_{km}$, where n_k is the number density of *k*-class structures. A second assumption neglects the convective part of Eq. (2) using the idea that the time scales associated with subgrid turbulent / molecular transport and chemical reaction are much shorter than those associated with convection. A third assumption considers only two size classes within the subgrid: *k* = 1 and 2, with *k* = 2 representative of the dissipative scales and *k* = 1 representative of scales between the cutoff scale and the dissipative scales. In conventional PaSR notation, *k* = 2 ≡ * and k = 1 ≡ 0. Because of the assumption of triadic interactions in Eq. (2), a connection with scales immediately larger than the cutoff scale can be included (red font below) – we consider this as *m* = 0 when expanding the sum in Eq. (2). Applying these assumptions leads to the following forms for k = 1 and k = 2:

$$\begin{aligned}
k=1:\ &\bar{\rho}[|\vec{v}'\cdot\vec{n}|_{(10)}+v_d^{(10)}](Y_s^{(1)}-Y_s^{(0)})A_{(10)}\\
&+\bar{\rho}[|\vec{v}'\cdot\vec{n}|_{(12)}+v_d^{(12)}](Y_s^{(1)}-Y_s^{(2)})A_{(12)}=\alpha_1\Omega\dot{\omega}_s(\bar{\rho},Y_s^{(1)},T^{(1)})\\
k=2:\ &\bar{\rho}[|\vec{v}'\cdot\vec{n}|_{(12)}+v_d^{(12)}](Y_s^{(2)}-Y_s^{(1)})A_{(12)}=\alpha_2\Omega\dot{\omega}_s(\bar{\rho},Y_s^{(2)},T^{(2)})
\end{aligned} \quad (4)$$

Using the interchange-with-the-mean definition (3) and substituting for the surface area yields the final algebraic form:

$$k=1:\ \bar{\rho}\frac{[|\vec{v}'\cdot\vec{n}|_{(10)}+v_d^{(10)}]}{L_{10}}(Y_s^{(1)}-Y_s^{(0)})+\bar{\rho}\alpha_2\frac{[|\vec{v}'\cdot\vec{n}|_{(12)}+v_d^{(12)}]}{L_{12}(1-\alpha_1)}(Y_s^{(1)}-\tilde{Y}_s)=\alpha_1\dot{\omega}_s(\bar{\rho},Y_s^{(1)},T^{(1)})$$
$$k=2:\ \bar{\rho}\alpha_2\frac{[|\vec{v}'\cdot\vec{n}|_{(12)}+v_d^{(12)}]}{L_{12}(1-\alpha_2)}(Y_s^{(2)}-\tilde{Y}_s)=\alpha_2\dot{\omega}_s(\bar{\rho},Y_s^{(2)},T^{(2)}) \quad (5)$$

A similar reduction process for the energy equation is needed to close the system. For now, we assume that the subgrid structure is adiabatic, which implies that

$$k=1:\ \bar{\rho}\frac{[|\vec{v}'\cdot\vec{n}|_{(10)}+v_d^{(10)}]}{L_{10}}(h(Y^{(1)},T^{(1)})-h^{(0)})+\bar{\rho}\alpha_2\frac{[|\vec{v}'\cdot\vec{n}|_{(12)}+v_d^{(12)}]}{L_{12}(1-\alpha_1)}(h(Y^{(1)},T^{(1)})-\tilde{h})=0$$
$$k=2:\ \bar{\rho}\alpha_2\frac{[|\vec{v}'\cdot\vec{n}|_{(12)}+v_d^{(12)}]}{L_{12}(1-\alpha_2)}(h(Y^{(2)},T^{(2)})-\tilde{h})=0 \quad (6)$$

Here, $h(Y,T)=\sum_s Y_s h_s(T)$, $h_s(T)=h_{0s}^f|_{\text{Tref}}+\int_{\text{Tref}}^{T}C_{p,s}(T)dT$ - NASA / Sandia curve-fits are used for this information. One can remark that, in the absence of coupling with scales larger than Δ, the structure of the *k* = 1 and *k* = 2 systems is identical – given externally-supplied filtered mean data $\bar{\rho},\tilde{Y}_s,\tilde{h}$, the solution of the systems yields $Y_s^{(1)}=Y_s^{(2)}$ and $T^{(1)}=T^{(2)}$. This also means that the closure for the filtered species production rates at the cutoff scale reduces as follows:

$$\overline{\dot{\omega}_s}|_{\text{PaSR}}=\alpha_1\dot{\omega}_s(\bar{\rho},Y_s^{(1)},T^{(1)})+\alpha_2\dot{\omega}_s(\bar{\rho},Y_s^{(2)},T^{(2)})=\dot{\omega}_s(\bar{\rho},Y_s^{(2)},T^{(2)})\ (\text{or}\ \dot{\omega}_s(\bar{\rho},Y_s^{(1)},T^{(1)})) \quad (7)$$

With outer-scale coupling, there will be differences between the *k* = 1 and *k* = 2 solutions. It should also be noted that the tandem solution of the *k* = 1 and *k* = 2 systems does not guarantee that $\tilde{Y}_s=\alpha_1Y_s^{(1)}+\alpha_2Y_s^{(2)}$ for *externally-supplied* filtered mean data. To ensure this, it is necessary to replace either the *k* = 1 or the *k* = 2 system with this constraint. This will lead to major differences in the solution for the replaced field – one that can significantly affect the calculation of the filtered production rates per Eq. (7). Most applications of algebraic PaSR techniques actually neglect the other contribution, modeling $\overline{\dot{\omega}_s}|_{\text{PaSR}}=\alpha_2\dot{\omega}_s(\bar{\rho},Y_s^{(2)},T^{(2)})$, where (2) is the retained field. The closure of the equation systems requires specification of L_{km}, $|\vec{v}'\cdot\vec{n}|_{(km)}$, and α_2, as discussed next.

2.2 PaSR Subgrid Closures

Several variants of PaSR-type subgrid closures have appeared in the literature. Here, we place three of them [1-3] in the notation defined above:

Sabelnikov and Fureby [1]:

$$|\vec{v}'\cdot\vec{n}|_{(12)}=u'_{rms}$$
$$L_{12}=\Delta/\widetilde{\text{Re}}_\Delta^{1/4}$$
$$\alpha_2=\max(0.01,\min(0.99,1.0/(1.0+\frac{L_{12}}{|\vec{v}'\cdot\vec{n}|_{(12)}}\frac{S_L^2}{\nu}))) \quad [S_L \text{ is the laminar flame speed}] \quad (8)$$

Magnussen (Eddy Dissipation Concept (EDC)) [2]:

$$
\begin{aligned}
&|\vec{v}'\cdot\vec{n}|_{(12)} = u'_{rms} \\
&L_{12} = \Delta / \widetilde{\mathrm{Re}_\Delta}^{1/2} \\
&\alpha_2 = \max(0.01, \min(0.99, \frac{1}{\widetilde{\mathrm{Re}_\Delta}^{3/4}}))
\end{aligned}
\tag{9}
$$

Giacomazzi, et al. [3]:

$$
\begin{aligned}
&|\vec{v}'\cdot\vec{n}|_{(12)} = u'_{rms} \\
&L_{12} = \Delta \\
&\alpha_2 = \max(0.01, \min(0.99, \max(\tilde{\alpha}_2 0.3183)));\ \tilde{\alpha}_2 = (0.3183\text{-}1.0)\widetilde{\mathrm{Re}_\Delta}/9.0 + (10.0\text{-}0.3183)/9.0
\end{aligned}
\tag{10}
$$

In these expressions, the turbulence Reynolds number is $\widetilde{\mathrm{Re}_\Delta} = \max(1.0, \mathrm{Re}_\Delta)$, $\mathrm{Re}_\Delta = u'_{rms}\Delta/\nu$. Limiting of this quantity and the range of the volume fraction is needed to avoid anomalous behavior when solving the equation systems discussed above. Neglecting coupling with the outer environment, it is clear that the system actually solved can be expressed as

$$
Y_s^{(2)} - \tilde{Y}_s = \frac{\tau}{\bar{\rho}}(1-\alpha_2)\dot{\omega}_s(\bar{\rho}, Y_s^{(2)}, \tilde{h});\quad \tau = L_{12}/(|\vec{v}'\cdot\vec{n}|_{(12)} + v_d^{(12)}) \tag{11}
$$

As the time scale τ becomes small or the volume fraction of $k = 2$ structures approaches unity, $Y_s^{(2)} \to \tilde{Y}_s$ and the closure approaches the 'laminar chemistry' model in which subgrid-scale information is neglected completely. As this time scale becomes large, the chemical production rate is driven to zero, and the result is the adiabatic equilibrium solution in which the forward and backward rates for all reactions balance. A small (net) chemical production rate therefore does not necessarily imply that the mixture is non-reactive – this makes the interpretation of certain outcomes of the analyses discussed subsequently somewhat challenging. The molecular diffusion velocity $v_d^{(12)}$ is normally omitted from PaSR-type closures – we have done the same for most of the studies shown later, but if included, the selected form is $v_d^{(12)} = \nu/\Delta$. Interactions with the outer environment, if included, are parameterized by the choices

$$
|\vec{v}'\cdot\vec{n}|_{(10)} = u'_{rms}\big|_{2\Delta},\ L_{10} = \Delta,\ v_d^{(10)} = \nu/\Delta,\ Y_s^{(0)} = \tilde{Y}_s\big|_{2\Delta},\ h^{(0)} = \tilde{h}|_{2\Delta} \tag{12}
$$

where the '2Δ' notation refers to the evaluation of the quantity by sampling data over a volume with lengths twice as large in all directions as the scale in question.

3 Results

3.1 MRA Database

The MRA procedure [4] as applied to one of the Sydney bluff-body stabilized flames (see Figure 1) is used to assess the potential of the above-mentioned PaSR closures in calculating the filtered production rates. Complete details of the MRA procedure, including a description of the numerical algorithms, can be found in [4] – some aspects are briefly described as follows. The equations are evolved as a large-eddy simulation using an implicit time-derivative preconditioning method. A low-dissipation PPM method is used to extend an all-speed version of NCSU's LDFSS [6] to higher order accuracy. The finest mesh is considered as the 'truth solution' for

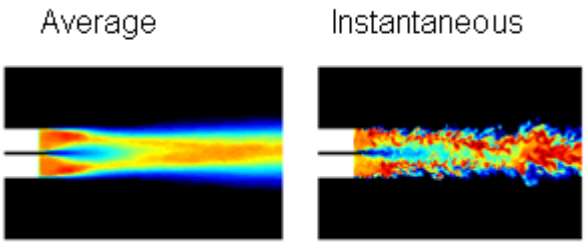

Figure 1: Fine-mesh average and instantaneous temperature distributions for a bluff body stabilized methane-hydrogen flame

evaluating the PaSR closures applied on coarser meshes – the 'laminar chemistry' model based on an 18-species reaction mechanism [7] is used to evaluate the reactive source terms and a simple WALE-type algebraic subgrid model is applied. Three mesh levels are considered, with the finest mesh (~113 M cells) resolved into the dissipative scales as discussed later. Two coarser meshes are generated by the successive removal of mesh cells in all directions.

For this problem, the extracted MRA database consists of 585 coarse-mesh locations, distributed throughout the region of mixing and reaction. For each coarse-mesh cell, we output flow properties from the cell itself and from the 26 face / edge / vertex neighbors of the cell. Underlying medium-mesh (8 × 27 cells) and fine-mesh (64 × 27 cells) information within this neighborhood is also outputted. Data is extracted for 886 time steps, meaning that the total amount of fine-mesh information outputted is 64 × 27 × 585 × 886 × NV, where NV is the number of flow properties. The flow properties outputted are the species densities (18), the velocity components (3), the density (1), the temperature (1), and the pressure (1), leading to NV = 24. In addition, geometric information suitable for calculating gradients at all mesh levels is also outputted.

Box-type volumetric filtering operators [4] are used to transfer the fine mesh data to the coarser mesh locations. Given that the fine mesh has a characteristic scale of Δ_f, the database is sufficient to examine the model responses at scales of $2\Delta_f$, $4\Delta_f$, $8\Delta_f$, and $12\Delta_f$, though only the first two are considered in this abstract. MRA-MSR also outputs *evolved* coarser-mesh data at each of the locations. This data is obtained by solving the Navier-Stokes equations on the coarser meshes with the velocity forcing term applied to constrain the eddy structures. At every coarser-mesh location, one can evaluate the chemical source terms using data filtered from the underlying finest mesh ('laminar chemistry' (LC)-filtered) or from the evolved coarser-mesh realization (LC-evolved). We have, from the finest mesh, values for $\bar{\rho}, \tilde{Y}_s, \tilde{h}$, and $\overline{\dot{\omega}_s}$. The first three drive the solutions for the balance equations listed

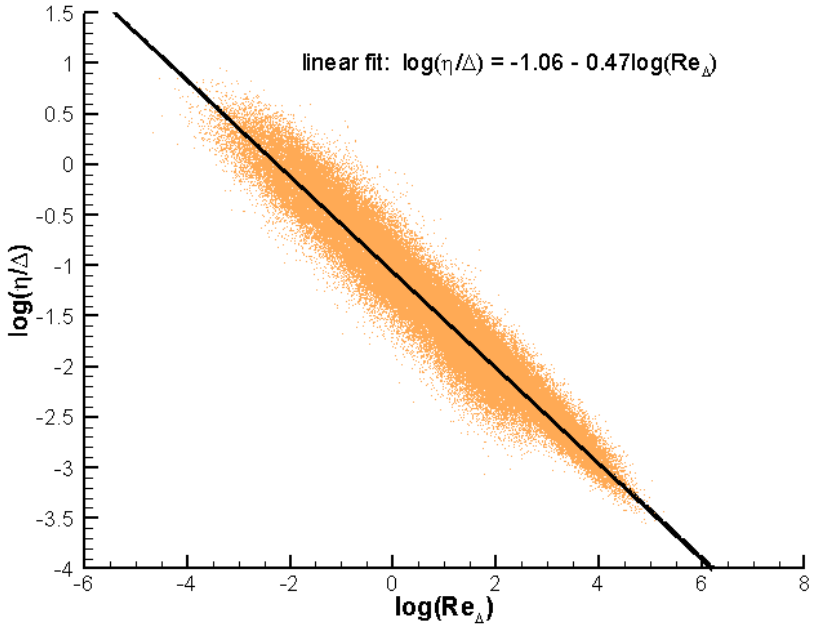

Figure 2: Normalized dissipative range length scale versus turbulence Reynolds number

above; the fourth (along with the heat release rate $\bar{q} = \overline{\sum_s \dot{\omega}_s h_s}$) are the target points for model assessment. Also from the finest mesh, we can calculate values for $u'_{rms} = \left(\overline{u_k^2} - \bar{u}_k^{\,2}\right)/3$ and $\nu = \bar{\mu}/\bar{\rho}$, where the overbars denote the application of the box filter.

3.2 Fine-Mesh Solution Assessment

The first set of results focuses strictly on the data from the finest mesh. Figure 2 shows a scatterplot of η / Δ versus Re_Δ on a log-log scale. Here, $\Delta = 2\Delta_f$ and $\Delta = 4\Delta_f$, corresponding to the medium and coarse meshes. The dissipative-range length scale is calculated using an assumed Kolmogorov scaling: $\eta = (\nu^3 / \varepsilon)^{1/4}, \varepsilon = \overline{\tau_{ij} S_{ij}} / \bar{\rho}$, where the overbar again denotes box-filtering at the medium and coarse-mesh scales. A linear scaling with an exponent of ~ -0.5 is evidenced, indicating that the finest mesh resolves down to the Taylor microscales but not to the Kolmogorov scales. Nevertheless, we will use dissipative-range (Kolmogorov) scaling to estimate velocity and time scales associated with resolved turbulence on the finest mesh.

An assumption inherent in PaSR closures is that reactivity is concentrated in the smallest scales of turbulence. To examine this assumption, we first extract the swirl strength λ_{ci} [6] and calculate its probability distribution, shown as the red curve in Figure 3 (right inner axis). For well-resolved isotropic turbulence, Chakraborty, et al. [8] associate the highest values of the swirl strength with the inverse of the dissipative-range time scale – we do the same here by correlating the extracted inverse dissipative-range time scales with the most probable values of the swirl strength (95% confidence interval). The conditional average of $\log_{10}(1/t_\eta)$ is plotted versus $S = \log_{10}(\lambda_{ci})$ as the green curve in Figure 3 (right outer axis). The range of $\log_{10}(1/t_\eta)$ corresponding to the most probable swirl strength values extends from ~3.5 to ~4.2 – this range is mapped back to the swirl-strength axis as the yellow

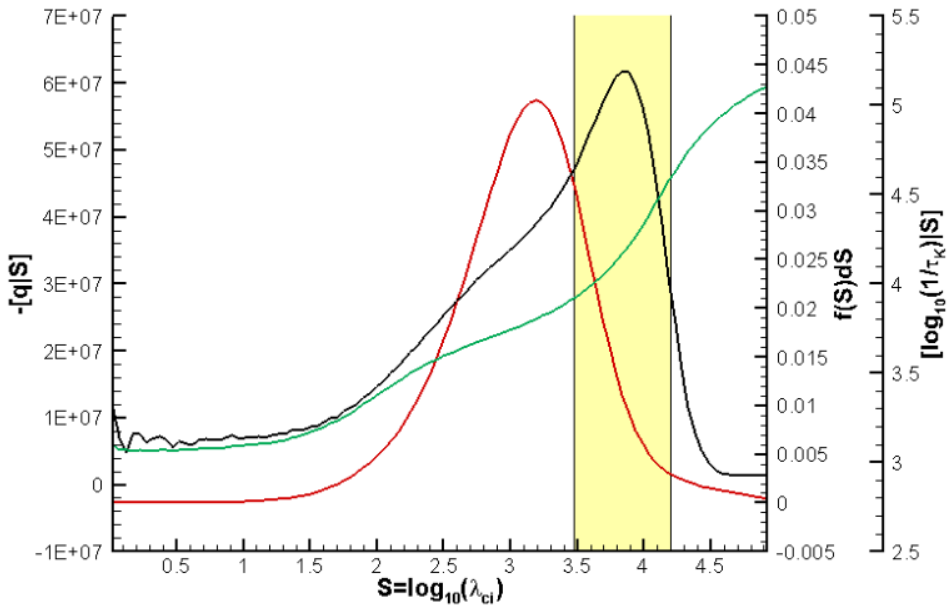

Figure 3: Heat release, dissipative scale, and swirl-strength probability distributions

solid region. Finally, the average of the heat release conditional on S is plotted as the black curve in Figure 3 (left axis). While it is clearly seen that peak heat release is associated with the dissipative range, the distribution of heat release is rather broad, indicating that localized reactivity is also present at larger turbulent scales.

3.3 PaSR Model Assessment

PaSR model predictions were first produced by solving Eqs. 5 and 6 at $\Delta = 2\Delta_f$ and $\Delta = 4\Delta_f$ as driven by information filtered from the finest mesh to these scales. A Newton iteration process was used, with the initial guess taken to be the composition and temperature filtered from the finest mesh. About 93% of the data locations yielded a converged, valid PaSR solution. Each of the models

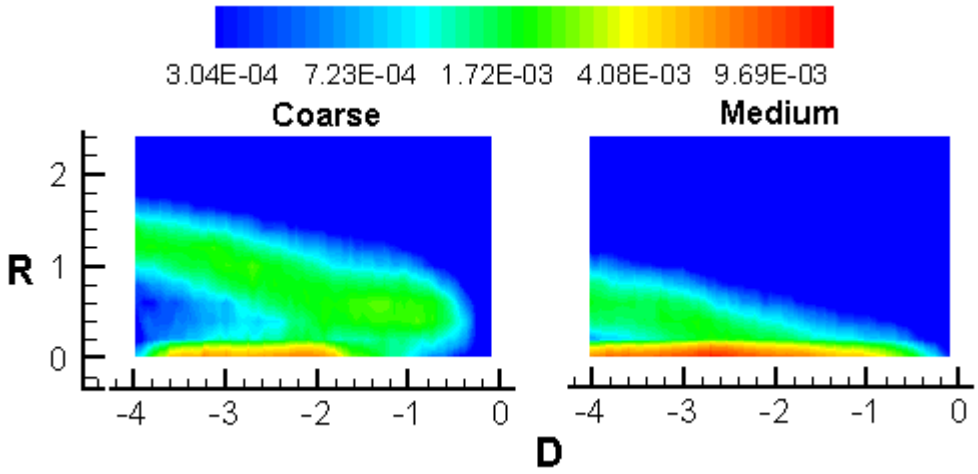

Figure 4: Joint probability distribution for Damköhler number and turbulence Reynolds number

mentioned (denoted henceforth as Fureby, Magnussen, and Giacomazzi) was analyzed, along with one example in which outer-environment information was allowed to influence the sub-grid balance equations (Magnussen's EDC formulation was employed in this case). As mentioned earlier, the target points for model assessment are the prediction of the filtered production rates (Eq. (7), quantified by the L_2 norm of the production-rate vector) and the associated heat release rate as compared to the same information filtered directly from the finest mesh. The scatter associated with the production-rate norm and the heat release is very large, and it is best to use logarithmic transformations and probability distributions to determine trends. We first define a Damköhler number as $\mathrm{Da} = \| \bar{\dot{\omega}} \| \Delta^2 / (\bar{\mu} \widetilde{\mathrm{Re}_\Delta})$ using filtered-fine mesh information. The base-10 logarithm of Da is denoted as D and the base-10 logarithm of $\widetilde{\mathrm{Re}_\Delta}$ is denoted as R. The sample space for D and R extends from -6 to 0 (100 bins) and 0 to 2.5

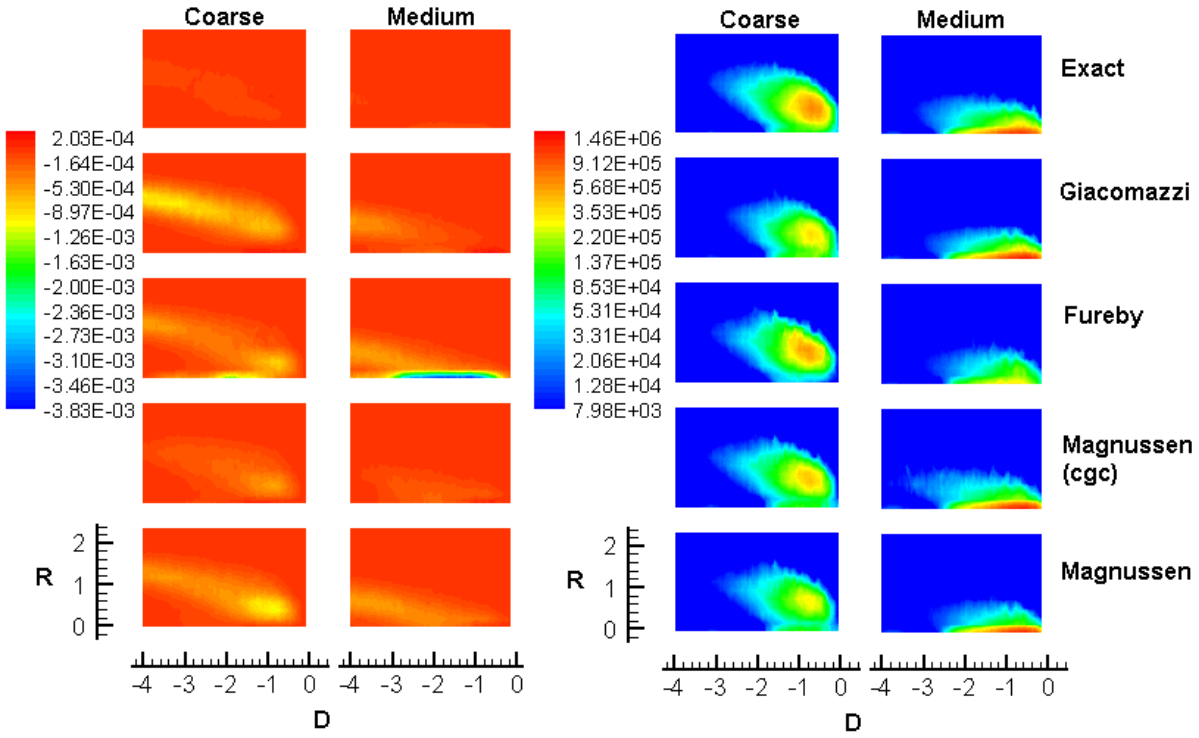

Figure 5: Production-rate norm ratio and heat release distributions over the Damköhler number / turbulence Reynolds number sample space

(14 bins). Figure 4 shows the joint probability distribution $f(D,R)dDdR$ for the coarse and medium meshes. The most obvious trend is that the probability distribution peaks at near unity values of the turbulence Reynolds number for both meshes but is more strongly associated with these values for the medium mesh. This implies that the medium mesh is still quite fine as far as resolution of the turbulence is concerned. The probability distribution also peaks at relatively small values of the Damköhler number (10^{-4} to 10^{-1}), implying that much of the flow is near equilibrium or non-reactive.

Figure 5 plots the conditional average of the base-10 logarithm of the production-rate norm ratio $\|\bar{\dot{\omega}}\|_{\text{PaSR}} / \|\bar{\dot{\omega}}\|$ (left set) and the conditional average of the heat release rate multiplied by the joint probability distribution ($-[q|S,R]f(S,R)dSdR$; right set) versus D and R for each mesh. The first measure indicates how well the PaSR variants locally predict the filtered species production rates; the second measure incorporates the joint probability distribution to indicate how well the models predict the overall heat release. The target point for the first measure is a uniform distribution of zero, implying an exact prediction of the production-rate norm over the entire D and R sample space. It is clear that none of the PaSR variants achieves this target and that the results among the models are somewhat inconsistent with respect to mesh resolution. For example, the Fureby model does reasonably well for the coarse mesh but performs poorly for the medium mesh at low values of the turbulence Reynolds number. The Giacomazzi and Magnussen models display an opposite trend, achieving a more uniform distribution on the medium mesh. The best results are obtained with the Magnussen model variant that incorporates outer-environment information (indicated as 'cgc' in the images). Positive values of the production-rate ratio are rarely observed for any of the models – the tendency is to under-predict local reactivity according to this measure, which as stated earlier, implies that the modeled system tends more toward adiabatic equilibrium. The target point for the second measure is the $\bar{q} = \overline{\sum_s \dot{\omega}_s h_s}$ distribution over the sample space (top image). Significant differences are observed in this metric between mesh levels, with the medium-mesh distribution peaking at turbulence Reynolds numbers near unity and the coarse-mesh results peaking at turbulence Reynolds numbers near ten. Both sets of data indicate that net heat release is most probably associated with higher values of the Damköhler number (10^{-2} to 1). Model predictions show similar trends as discussed earlier, with the Magnussen (cgc) variant providing the best agreement with the target distributions. All models capture the general shapes of the heat release rate distributions.

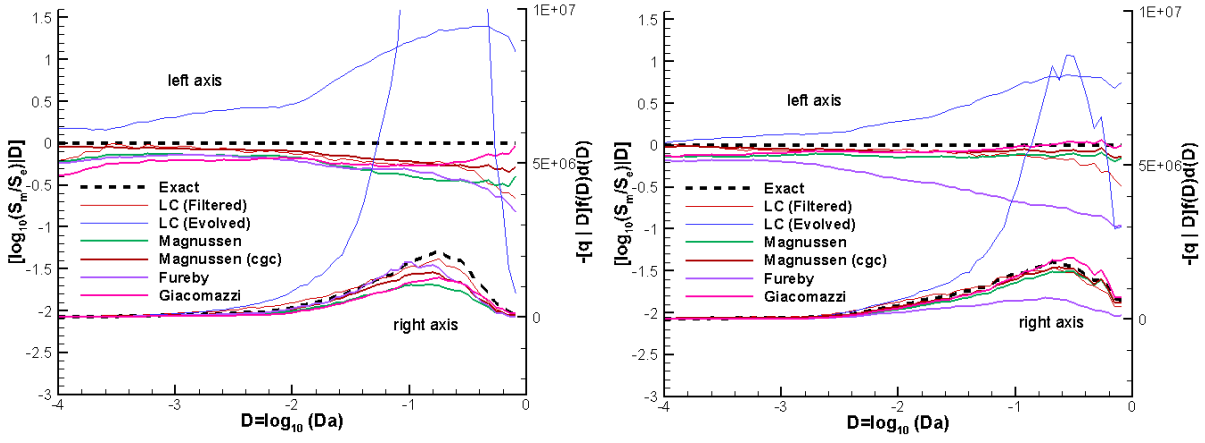

Figure 6: Production rate norm ratio and heat release rate versus Damköhler number (left-coarse mesh; right – medium mesh)

Similar information is shown in Figure 6, but here, the distributions are integrated over the sample space of the turbulence Reynolds number, producing quantities conditioned only on D. Figure 6 also shows results from the two 'laminar chemistry' models discussed earlier – one in which the production

rates are evaluated using filtered mean data ($\tilde{Y}_s$, $\tilde{T}$) from the finest mesh (LC-filtered) and the other in which they are evaluated using data evolved on each of the coarser meshes (LC-evolved). Target distributions for the production-rate norm ratios and the heat release rate are indicated as dashed black lines. The LC-filtered solution shows large errors in both measures – this is indicative of the fact that the perturbed system of reactions is given no opportunity to relax back to a (partial) equilibrium state. In an actual calculation using LC, this opportunity would be present, and the failures indicated above might not be realized. This is evidenced rather strongly when the source terms are calculated using the evolved data – the errors are much lower, as this system (by construction) has had the opportunity to return to (partial) equilibrium. The LC-evolved predictions for the heat release rate distribution are perhaps the best of any of the approaches, but the reduction in the norm-ratio measure at high Damköhler numbers may be indicative of too rapid of a return to adiabatic equilibrium. The predictions from the PaSR variants follow the same trends as discussed earlier, with the largest deviation from the 'exact' result shown for the Fureby formulation on the medium mesh. The main reason is that the definition for α_2 does not return to near unity for unity values of the turbulence Reynolds number, which are most probable for the medium mesh. This means that the sub-structure balance equations are more dominated by the reaction source term, which tends to relax the system toward a state of adiabatic equilibrium.

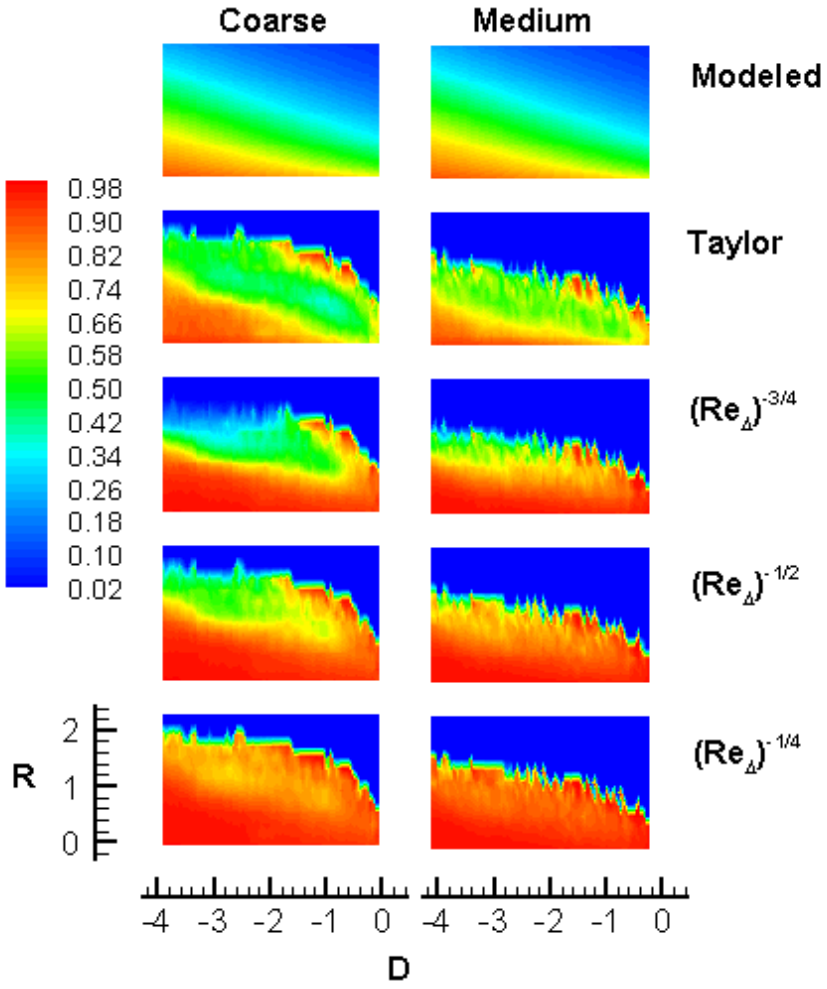

Figure 7: Conditional average of the optimal α_2 over the Damköhler number / turbulence Reynolds number sample space

3.4 PaSR Model Optimization

As discussed earlier, an algebraic PaSR method is most sensitive to the product $\tau(1-\alpha_2)$. Specific values for the time scale τ relate to the choices of characteristic subgrid velocity and length scales – such choices can be parameterized as functions of the turbulence Reynolds number: $\tau = \Delta(\widetilde{\mathrm{Re}}_\Delta)^m / u'_{rms}$. The proper expression for the volume fraction α_2 is much less certain. This quantity is the product of the number density of k = 2 class structures and the size of such structures. While the latter might be estimated, the former is unknown and could change significantly through chemical reaction and other processes. One way to arrive at a suitable form for α_2 is by an optimization process. Here, we consider three choices for the exponent m above: m =-1/4, m=-1/2, and m=-3/4 as well as one choice for the time scale motivated by the availability of dissipative-range information from the finest mesh: $\tau = \eta / (\nu/\Delta + \nu/\eta)$ (referred to as the 'Taylor' choice). The optimization process varied α_2 from 0.01 to 0.99 in increments of 0.01, solving the PaSR subsystem and determining the *rms* error in the source term vector, relative to the filtered fine-mesh solution: $[\sum_s (\overline{\dot{\omega}_s}\,|_{\mathrm{PaSR},\alpha_2} - \overline{\dot{\omega}_s})^2]^{1/2}$. The value of α_2 that minimized the error for a given location and time was then outputted. A location and time were discarded if less than 25 of the α_2 values led to a solvable PaSR system. One result of the optimization process is the conditional average of α_2 as a function of D and R, shown in Figure 7 for different choices of the time scale τ. The optimal value of α_2 is biased toward unity for all modeled choices of the time scale. The Taylor choice, which uses dissipative-range information directly, produces a more non-uniform distribution, showing a reduction in α_2 for higher values of the turbulence Reynolds number and Damköhler number. Compared with the other choices, the distributions of α_2 are also more similar between mesh levels. The top-most part of the figure shows the results of a simple curve-fit to the Taylor distributions:

$$\alpha_{2,\mathrm{mod}} = 1.0 / (1.0 + \mathrm{Da}^{0.175}(\widetilde{\mathrm{Re}}_\Delta - 0.75)^{1/2}) \qquad (13)$$

This parameterization is similar to that of Sabelnikov and Fureby [1] in that it includes both chemical and mixing time scale information. Figure 8 shows predictions from each of the optimal PaSR variants, again plotted versus D. A modeled Taylor form, which uses Eq. (13) along with the curve-fit shown in Figure 2 for the dissipative length scale ($\ln(\eta/\Delta) = -1.06 - 0.47\ln(\mathrm{Re}_\Delta)$), is also included in the comparison. All optimal variants show a significant improvement in predictive capability, relative to the original models (Figure 6), but the best results are provided by the Taylor choice. The modeled

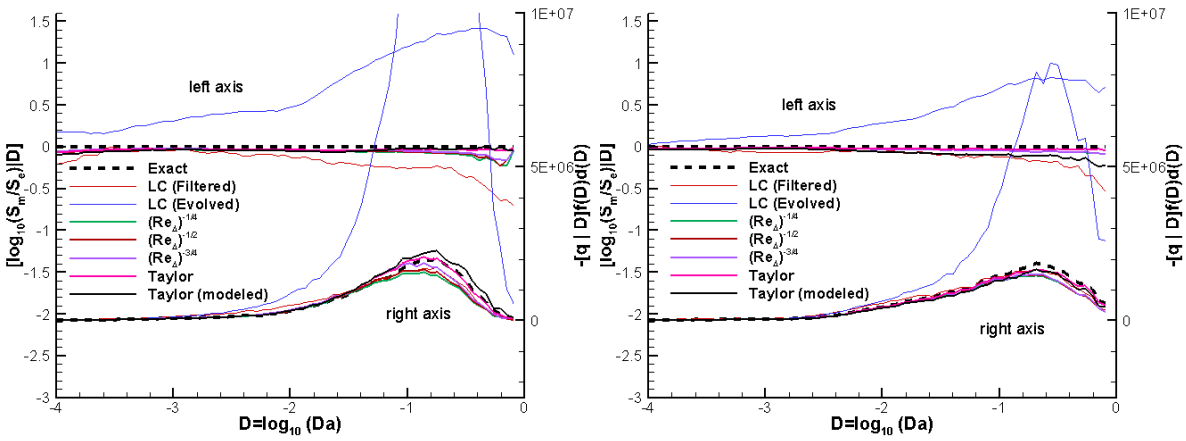

Figure 8: Production rate norm ratio and heat release rate versus Damköhler number – optimal PaSR variants (left- coarse mesh; right – medium mesh)

Taylor form also performs well but slightly over-predicts the heating-rate distribution on the coarse

mesh. The sensitivity of the predictions to the mesh resolution is greatly reduced, relative to the baseline models.

4 Conclusion and Future Work

This work has used hierarchical databases extracted from NCSU's MRA-MSR technique to analyze the performance of several algebraic PaSR closures for the filtered species production rates. Conditional distributions of measures of reactivity over the Reynolds number / Damköhler number sample space have been developed providing a 'visual' indication of the performance of a subgrid closure relative to a target solution. None of the tested variants accurately predicts species production or heat release as obtained by explicitly filtering fine-mesh data. 'Optimal' PaSR forms, derived by interrogating the fine-mesh database, perform much better and display a degree of mesh independence that is not found in the baseline models. While the optimal forms determined through this analysis may be case-specific, the potential of MRA-MSR in revealing such information and in providing directions for model improvement is apparent. The key result is that the length / time scale information supplied to algebraic PaSR models should be mostly associated with the dissipative range of the energy spectrum, and that better models for such, extractable from resolved-scale information, could lead to general improvements in predictive capability. An outstanding issue in the analysis procedure is the use of the net chemical production rates in defining the Damköhler number – it appears important to distinguish between low net production rates due to attainment of chemical equilibrium and those due to non-reactivity. Ongoing work in this area is focused on generalizing the MRA procedure to enable several TCI models to be assessed simultaneously on different mesh levels, applying it to supersonic combustion problems, and integrating the performance assessment measures into the code so that the outcome of a particular simulation includes the conditional probability distributions.

References

[1] Sabelnikov, V. and Fureby, C. "LES Combustion Modeling for high Re flames using a Multi-Phase Analogy" *Combustion and Flame,* Vol. 160, 2013, pp. 83-96.

[2] Fureby, C. "Large eddy Simulation Modelling of Combustion for Propulsion Applications," Philosophical Transactions of the Royal Society A, Vol. 367, 2009, 2957–2969.

[3] Giacomazzi, E., Bruno, C., and Favini, B. "Fractal Modeling of Turbulent Combustion", *Combustion Theory and Modeling*, Vol. 4, No. 4, 2000, pp. 391-412.

[4] Edwards, J.R. and Nielsen, T. "Mesh-Sequenced Realizations for Evaluation of Subgrid-Scale Models for Turbulent Combustion" *AIAA Journal*, Vol. 58, No. 11, pp. 4878-4892.

[5] Patton, C. and Edwards, J.R. ""Least Squares Minimization Closure Models for LES of Turbulent Combustion" *Flow, Turbulence and Combustion,* Vol 102, No. 3, 2019, pp. 1-35.

[6] Edwards, J.R. "Towards Unified CFD Simulations of Real Fluid Flows," AIAA Paper 2001-2524, 2001.

[7] Larsson, A., Zettervall, N., Hurtig, T, Nilsson, E.J.K., Ehn, A., Petersson, P., Alden, M., Larfeldt, J., and Fureby, C. "Skeletal Methane-Air Reaction Mechanism for Large Eddy Simulation of Turbulent Microwave-Assisted Combustion" Energy Fuels, Vol. 31, No. 2, 2017, pp. 1906-1926.

[8] Chakraborty, P, Balachandar, S, and Adrian, R. "On the Relationships between Local Vortex Identification Schemes," *Journal of Fluid Mechanics,* Vol. 535, 2005, pp. 189-214.